AGU ADVANCING EARTH AND SPACE SCIENCE

Geophysical Research Letters

RESEARCH LETTER
10.1029/2021GL093043

Improving the Resolving Power of InSAR for Earthquakes Using Time Series: A Case Study in Iran

F. Liu[1], J. R. Elliott[1], T. J. Craig[1], A. Hooper[1], and T. J. Wright[1]

[1]School of Earth and Environment, COMET, University of Leeds, Leeds, UK

Key Points:

- Using time series analysis, we can detect small coseismic displacements that are not readily visible or ambiguous in single interferograms
- Earthquakes occurring close in time and space can be separated by a time-dependent parameterized model fitted to Interferometric Synthetic Aperture Radar time series analysis
- We can achieve more robust and seismologically consistent earthquake modeling results by using a time series approach

Supporting Information:

Supporting Information may be found in the online version of this article.

Correspondence to:

F. Liu,
eefl@leeds.ac.uk

Citation:

Liu, F., Elliott, J. R., Craig, T. J., Hooper, A., & Wright, T. J. (2021). Improving the resolving power of InSAR for earthquakes using time series: A case study in Iran. *Geophysical Research Letters*, *48*, e2021GL093043. https://doi.org/10.1029/2021GL093043

Received 22 FEB 2021
Accepted 23 JUN 2021

Abstract Interferometric Synthetic Aperture Radar (InSAR) is an established method to measure earthquake surface displacements. However, due to decorrelation and atmospheric noise, only a certain fraction of earthquakes is readily observable with single interferograms. To enhance the potential of retrieving InSAR earthquake observations, we apply InSAR time series analysis and use several recent earthquakes (M_w 5.6–6.3, 2018–2019) in Iran as case studies. We find that the coseismic displacement signals of these earthquakes, which might not be discernible within single interferograms, are better resolved using our approach. We reconstruct the coseismic deformation fields by fitting surface displacements using a time series approach. We find that the reconstructed coseismic deformation fields yield more robust and seismologically consistent earthquake modeling results when compared to single coseismic interferograms. Our work suggests that a time series approach is an effective way to improve the resolving power of InSAR for earthquake studies.

Plain Language Summary Earthquakes cause the ground to temporarily shake, but also result in permanent movement of the surface of the Earth. This surface displacement can be detected using sensitive radar echoes from satellites when it is large enough. By differencing phases of radar images from before and after the earthquake (a technique known as interferometry), it is possible to detect where an earthquake has happened and determine its source parameters. However, the atmosphere and different imaging conditions cause noise in individual interferogram images, masking the earthquake movement. Here, we use a method involving a time series of multiple images before and after the earthquake to improve the picture of the earthquake by observing how the estimates of ground movement change through time. We therefore improve measurement of the distribution and amount of ground movement, allowing the detection of smaller earthquakes than before. Using a sequence of recent earthquakes in Iran as a test case, our method improves the assessment of the type and the location of detected earthquakes compared with single image interferogram data (average 36% uncertainty reduction), with the validation from seismic data. Our work demonstrates the enhancement of this time series approach and its potential in future earthquake studies.

1. Introduction

With the advancement of Synthetic Aperture Radar (SAR) satellite missions, Interferometric SAR (InSAR) has become an established method to measure the Earth's surface deformation caused by earthquakes, greatly improving our ability to observe active tectonic processes (Elliott et al., 2016; Massonnet et al., 1993; Peltzer & Rosen, 1995; Salvi et al., 2012). InSAR offers an alternative approach, other than seismology, to provide independent measures of fault location, depth, and orientation (e.g., Lohman & Simons, 2005; Pedersen et al., 2003). Unfortunately, due to the dominant error sources within InSAR data of decorrelation and atmospheric noise (Agram & Simons, 2015; Zebker et al., 1997), only earthquakes above a certain size or that are shallow enough can be observed. Recent studies exploit the potential of the latest SAR satellites using single interferograms to detect earthquakes in the first instance (e.g., Funning & Garcia, 2019; Morishita, 2019), but the overall detectability of earthquakes by this approach is inconsistent and non-robust, and subject to extremely high failure rates (49% failure for Sentinel-1 and 23% failure for ALOS-2).

This circumstance makes using InSAR for earthquake studies challenging, especially for small earthquakes (M_w 5.0–6.5, from a geodetic point of view) due to their weak signals, despite in some cases still causing fatalities when close to population centers (England & Jackson, 2011). However, there is merit in trying to increase the sensitivity of our observations, as we can draw inferences from a huge number of small

earthquakes assuming their behavior scales similarly with large ones (Ide, 2019). Additionally, by precisely locating these small earthquakes, it may be possible to link seismic activity directly with active fault structures that are capable of larger earthquakes.

To achieve more accurate and robust measurements, InSAR time series analysis has been previously proposed (Crosetto et al., 2016; Hooper et al., 2012; Jolivet et al., 2012; Osmanoğlu et al., 2016). Phase-stable or high-coherence pixels are identified to reduce the decorrelation noise (e.g., Ferretti et al., 2011; Samiei-Esfahany et al., 2016), and spatiotemporal filtering is applied with the optional implementation of a tropospheric correction to lower the impact of atmospheric noise (e.g., Dalaison & Jolivet, 2020; Doin et al., 2009; Goldstein & Werner, 1998; Li et al., 2005; Pepe et al., 2015). Some recent cases show that InSAR time series analysis, which has been used to measure small amplitude, long duration ground displacements associated with interseismic strain accumulation, postseismic deformation, and shallow creep (Fialko, 2006; Hilley et al., 2004; Ryder et al., 2007), has the capability to extract coseismic signals from various sources of noise (Fielding et al., 2017; Grandin et al., 2017), suggesting a promising way for enhancing earthquake detection using InSAR.

To fully exploit the potential of InSAR in earthquake detection and modeling, we perform InSAR time series analysis of Sentinel-1 data and focus on three recent earthquakes (M_w 5.6–6.3, ~10 km depth) in south-western Iran as case studies. The Arabia–Eurasia collision causes numerous large earthquakes that have been recorded in history (Ambraseys, 2001) and long-lived postseismic afterslip from more recent observed events in this broad deformation zone (Copley et al., 2015; Copley & Reynolds, 2014). On November 12, 2017, the large M_w 7.3 Ezgeleh–Sarpolzahab earthquake struck this region, triggering many aftershocks and long-lived postseismic deformation in the area surrounding the mainshock (Barnhart et al., 2018; Feng et al., 2018; Nissen et al., 2019). We focus on three notable late aftershocks as examples (M_w 6.0, M_w 6.3, and M_w 5.6 earthquakes, which happened on August 25, 2018, November 25, 2018, and January 6, 2019, respectively). We process five years of Sentinel-1 observations over this area, from November 2014 to September 2019 to ensure enough data is available to constrain potential secular and annual deformation (Figure 1), and reconstruct the enhanced coseismic deformation field using a parameterized function describing surface displacement to time series data. We use independent seismological observations and a recent geodetic solution (Fathian et al., 2021) to validate our approach. We find that our deformation fields better constrain the source models and are more consistent with seismological data compared to those using single interferograms.

2. Methodology

Using Sentinel-1 Single Look Complex images, we form interferograms with multilooking (4 in azimuth and 20 in range yielding a pixel size of ~50 × 60 m^2) and spatial filtering using the LiCSAR processor chain (Lazecky et al., 2020). The DEM used during the processing is Shuttle Radar Topography Mission 3 s. We form interferogram networks by connecting each image to three subsequent acquisitions and use the StaMPS software (Hooper et al., 2007) to perform time series analysis, including GACOS corrections for tropospheric artefacts using the TRAIN software (Bekaert et al., 2015; Yu et al., 2018).

For earthquake studies, InSAR time series analysis leads to frequent estimates of surface displacement through time, providing better noise resilience. Compared to single interferograms, we can improve earthquake detection and the quality of coseismic surface deformation measurements in time series, especially when the deformation signals are obscured by decorrelation or atmospheric noise. Additionally, we can separate multiple earthquakes which occur close in time and space (e.g., the M_w 6.3 and M_w 5.6 earthquakes are separated by only 42 days and 30 km) through data fitting to time series (Figure 2).

Having established that a coseismic signal is discernable in time series, further improvements can be made if we assume a deformation model appropriate for displacements due to the seismic cycle. We can reconstruct the coseismic deformation field via a time series approach similar to that used in GNSS (Heflin et al., 2020; Tobita, 2016). Considering deformation associated with the seismic loading cycle, we assume that surface deformation at time t following an earthquake at time t_0 can be decomposed as follows:

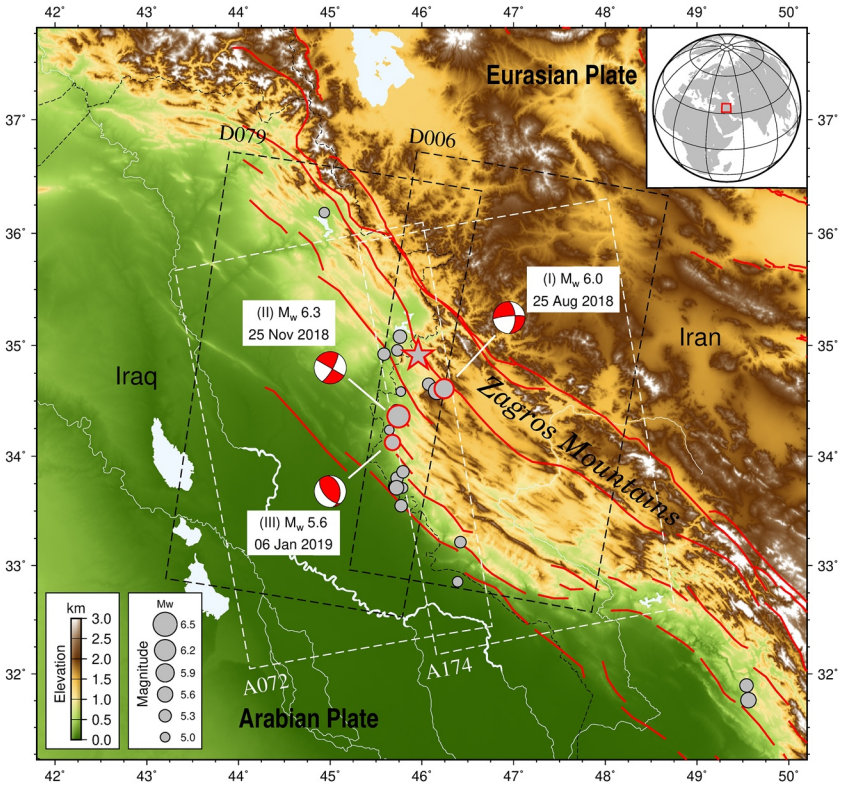

Figure 1. Topographic map of the Iran–Iraq border area. The epicenter of the large M_w 7.3 earthquake from November 12, 2017 is shown by the red star, the three study cases are indicated by focal mechanisms, and all other $M_w \geq 5.0$ earthquakes from the United States Geological Survey catalog are represented by gray circles (spanning November 2014–September 2019). The white and black dashed rectangle boxes show the area of processed Sentinel-1 data from two ascending tracks (A072 and A174) and two descending tracks (D079 and D006). Red lines show major active faults (Styron & Pagani, 2020).

$$\psi(t) = \mathrm{H}(t - t_0)\left[C + A\ln\left(1 + \frac{t}{\tau}\right)\right] + Vt + b \tag{1}$$

where $\mathrm{H}(*)$ is a Heaviside step function, C represents the coseismic displacement, A and τ are the parameters for a logarithmic function representing the postseismic deformation (Ingleby & Wright, 2017; Liu & Xu, 2019), V is the long-term linear deformation rate which contains in part the interseismic displacement, and b is a constant reference offset in observations.

Whilst postseismic deformation may occur following all earthquakes, we only consider the dominant postseismic deformation of the M_w 7.3 mainshock, as the three aftershocks we focus on are either relatively small in magnitude or occurred too close in time or space, impeding for robust postseismic fitting. Although this simplification will lead to the inclusion of some early postseismic motion into the reconstructed coseismic deformation fields, the InSAR derived magnitude and moment from our approach (Table S1) is consistent with seismological observations, illustrating this effect is limited in these cases. Other smaller events occurred close to our study cases but cannot be distinguished in time series either because they are too small or too close to other larger-magnitude earthquakes. Additionally, since the deformation signals of the three study cases are coincident in time (Figure 2b), we fit all three aftershocks in one equation. The model we used in this study is then:

$$\psi(t) = \mathrm{H}(t - t_1)\left[C_1 + A\ln\left(1 + \frac{t}{\tau}\right)\right] + \sum_{i=2}^{n}\mathrm{H}(t - t_i)C_i + Vt + b \tag{2}$$

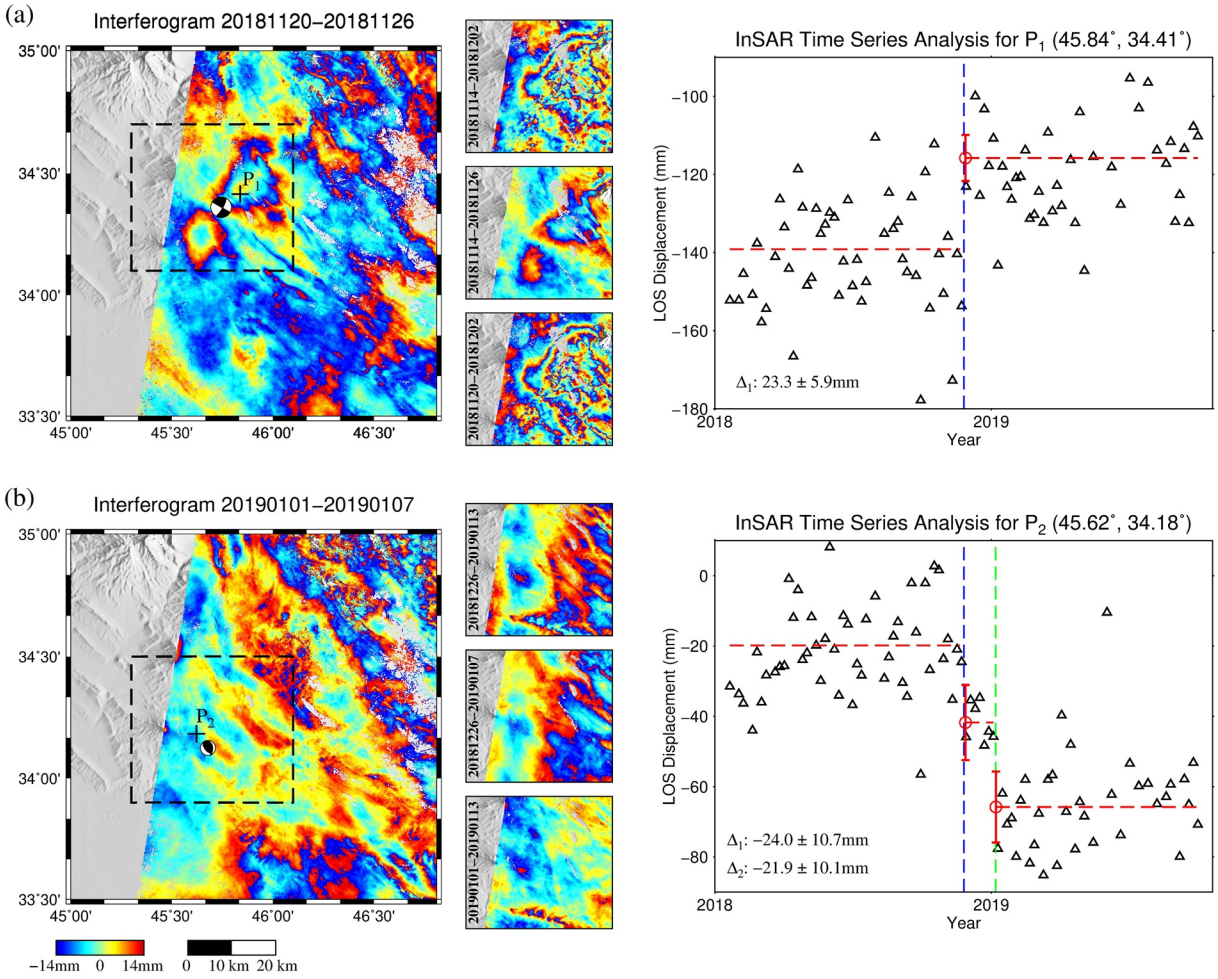

Figure 2. Interferometric Synthetic Aperture Radar (InSAR) time series analysis improvements to earthquake detection, using the M_w 6.3 and M_w 5.6 earthquakes on track D006 as examples. The tropospheric noise has been corrected using GACOS. (a) Left: the shortest (6 days) interferogram covering the M_w 6.3 earthquake, and three longer interferograms (acquisition dates are indicated by the title) of the area covering the earthquake deformation marked by the dashed rectangle. Right: time series analysis for a representative peak displacement pixel P_1. Blue vertical dashed line represents the event time of the M_w 6.3 earthquake. Red horizontal dashed lines show a simple step function fitting of the data, and the values of the offsets (delta) and error bars are shown at the lower-left corner. (b) Same as (a) but for the M_w 5.6 earthquake and pixel P_2, green vertical dashed line represents the event time of the M_w 5.6 earthquake.

where t_i and C_i represent the event time and the coseismic deformation of each earthquake sorted by time ($n = 4$ in this study, with first event at t_1 denoting the mainshock).

We first use maximum likelihood approach to determine the postseismic time τ and find it can be a constant value (~6 days) in our study (Figure S1). We then reduce the fitting of Equation 2 to a linear inverse problem and evaluate the other parameters and their uncertainties (Figures S2–S4).

3. Results

3.1. Coseismic Deformation Reconstruction

Our reconstructed coseismic deformation fields improve the detectability of earthquakes (Figures 3 and S5), and obtain higher signal-to-noise ratios (SNRs) as indicated by the reduced noise observed in the semi-variogram fitting (Webster & Oliver, 2007; Figure S6). The coseismic deformation signals are clearer and more easily recognizable after reconstruction, especially on the ascending track. Here we take the most challenging M_w 5.6 earthquake (given its small magnitude) as an example. On both ascending and descending tracks, the deformation signals in the interferograms are masked by strong atmospheric noise, but are not

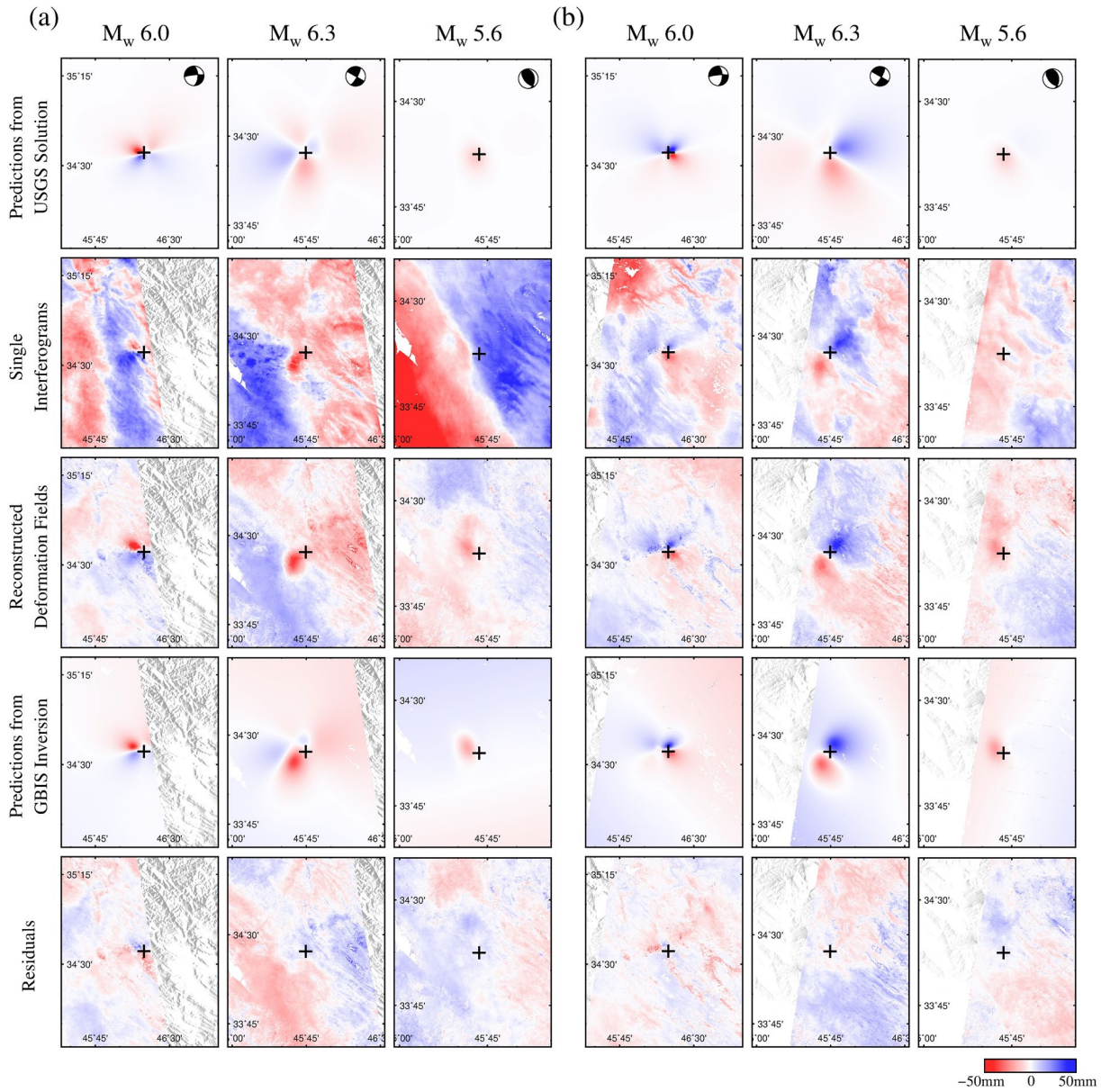

Figure 3. Comparison between the shortest interferograms and the reconstructed deformation fields. For the prediction from United States Geological Survey (USGS) solution, we assume a uniform dislocation embedded in an isotropic elastic half-space (Okada, 1985), faults are equal in width and length, and the slip-to-length ratio is set to 6×10^{-5} for these intraplate earthquakes (Scholz, 2002). The plus symbols indicate the epicenter of the focal mechanism from USGS solution. (a) Data from track A072. From top to bottom, the rows represent the predictions from USGS solution, the single interferograms, the reconstructed deformation fields, predictions from GBIS inversion (Bagnardi & Hooper, 2018), and the residuals between the reconstructed deformation fields and the predictions from GBIS inversion, respectively. (b) Same as for (a) but for track D006.

quite weak enough to be completely invisible upon examination of multiple interferograms (Figure 2b). After reconstruction, we successfully make the earthquake signal more readily apparent for identification, resolving the ambiguity of whether it is associated with an earthquake deformation signal or solely atmospheric noise. Additionally, we can see that the deformation pattern in the reconstructed signal becomes more similar to the expected deformation, shown in the forward modeling (based upon the seismological catalog focal plane solution), implying a more seismologically consistent earthquake model.

3.2. Earthquake Modeling

We first downsample the data, reducing the number of pixels to ~500, with a greater pixel density in the nearfield (Figure S7). Then we use the GBIS software (Bagnardi & Hooper, 2018) to provide a uniform fault plane slip solution with uncertainties to ascertain the improvement gain in constraining fault parameters from our reconstructed deformation fields, and compared to independent seismological observations and a recent InSAR solution (Fathian et al., 2021). A common issue when modeling small or buried earthquakes that do not rupture up to the surface, is that a focal plane ambiguity remains in InSAR solutions (as it does in seismologically determined solutions). Here we try to model both focal planes and select the one which provides a normally distributed output of strike values (M_w 6.0 and M_w 6.3) or more seismologically consistent solution (M_w 5.6).

The geodetic solutions from our data (Figure 4 and Table S1) show that although there are some discrepancies (e.g., rake value for the M_w 6.0 earthquake), they agree well with the seismological observations, and the modeling results from our time series approach are more seismologically consistent (average 18% vs. 22% relative changes). More importantly, reconstructed deformation fields provide better-constrained solutions, with an average of 36% narrower confidence interval (CI) for all three earthquake parameters. The M_w 6.0 earthquake achieved the most obvious gains (average 56% CI reduction) as the deformation signals are more distinct after reconstruction. The M_w 6.3 earthquake, whose signals are already clear before reconstruction, has the least difference modeling results (1% relative change) while our approach gives significant CI reduction (average 26%). Conversely, the solution of the M_w 5.6 earthquake, whose signals have been greatly enhanced following our approach, is still relatively poorly constrained. With only one elliptical lobe being clearly observed, it becomes difficult to constrain the fault geometry well (large uncertainties for strike and rake values). This reemphasizes the limitation of surface displacements in constraining geometry and resolving the focal plane rupture ambiguity when the rupture is buried and does not break the surface, even with improved SNR (Biggs et al., 2006; Elliott et al., 2010). Additionally, our approach achieves similar fault parameters and uncertainties as that from Fathian et al., (2021) for the already visible M_w 6.3 earthquake, whilst also providing significant improvements for the M_w 6.0 earthquake (Table S1).

The better-constrained result from depth and location measurements shows the advantage of InSAR observations (especially for time series, Figure S8). Routine depth measurements for shallow continental earthquakes from the seismological observations contain values probably fixed *a priori* (such as 10 km depth for the M_w 6.0 earthquake from USGS catalog). Although the true values cannot be known without additional near-field constraints such as a dense aftershock survey, our approach provides better-constrained locations, and more informative depth measurements with uncertainties for shallow events.

3.3. Comparison With Stacking

Stacking is another method to improve the SNR of InSAR data, which can also be helpful in extracting the coseismic deformation of small earthquakes (e.g., Luo et al., 2021; Qian et al., 2019). We perform stacking using all reconstructed pairs of pre- and post-event acquisitions to derive the coseismic deformation (Text S1), and compare it to our approach (Figures S9 and S10).

Overall, stacking achieves a similar SNR to our reconstructed deformation fields, while our approach provides more robust earthquake modeling (average 17% CI reduction). Noticeably, the magnitude of the M_w 6.0 earthquake from stacking is biased larger than our approach, compared to the results of the other two earthquakes. We believe this is because the postseismic deformation of the mainshock is contained in the stacked results (Figure S11), although we use observations 6 months later than the mainshock to perform stacking. This shows the larger impact from the postseismic deformation of the mainshock than the early postseismic motions of the aftershock in our model, and highlights a significant advantage of our approach that such bias can be reduced when modeling the aftershocks.

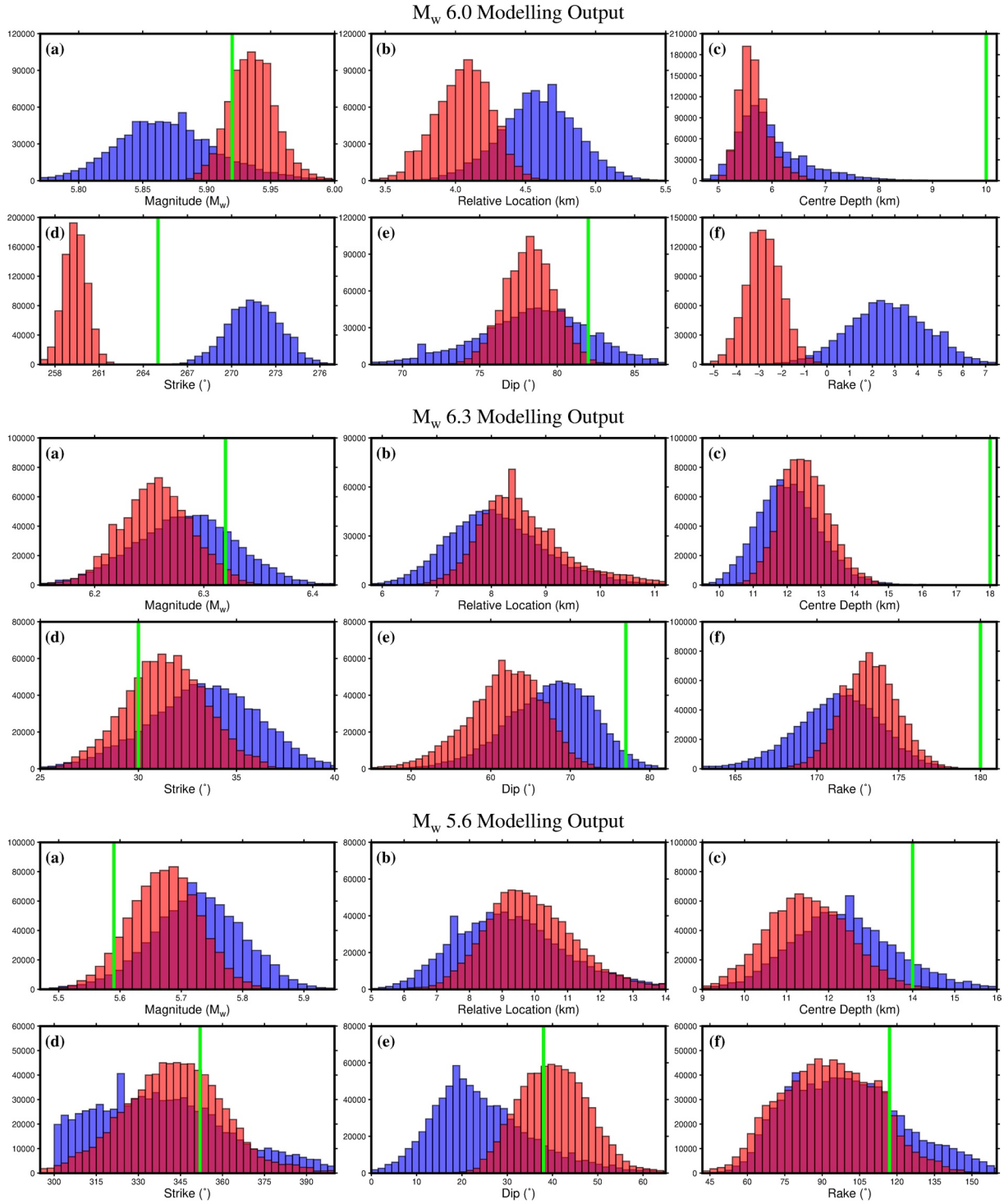

Figure 4. Modeling outputs for selected fault parameters. Red and blue bins represent the distributions from the reconstructed deformation fields and the shortest interferograms, respectively. Green lines are the United States Geological Survey (USGS) solutions (note the rake value for the M_w 6.0 event is −31°). (a) Earthquake moment magnitude. (b) Relative location, the horizontal distance between the InSAR derived source location and the epicenter of USGS (not indicated by green lines as zero reference value). (c–f) Fault plane center depth, Strike, Dip, and Rake values.

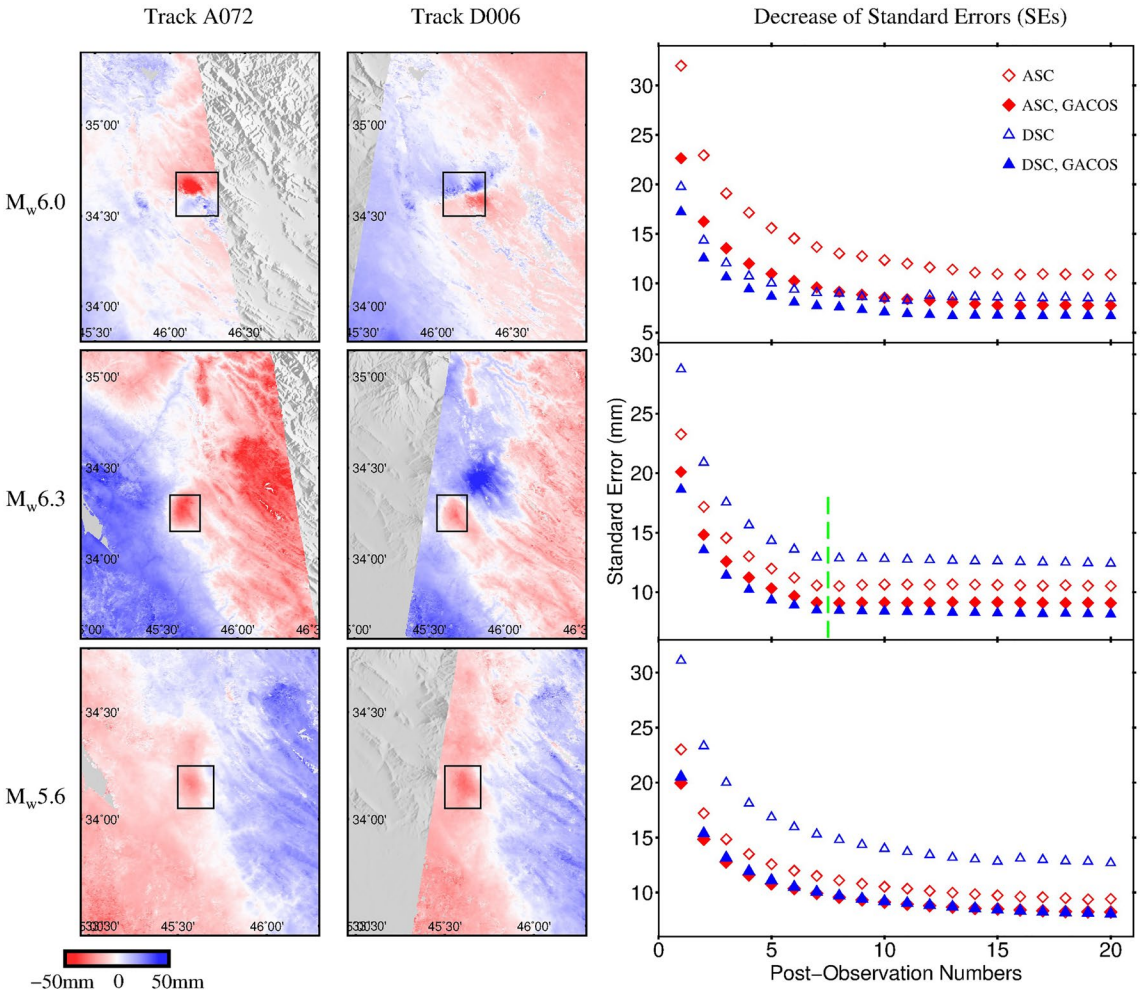

Figure 5. The impact of the number of post-observations used in time series and application of GACOS corrections on the quality of coseismic displacement reconstruction. For each row we show the optimal reconstructed deformation fields (using all our data) from two tracks without GACOS correction, and the corresponding decrease (proportional to $1/\sqrt{N}$) of the standard errors (SEs) as the post-observation numbers increase (using all pre-observations, ~100 images). We show the mean SE values of all pixels within the black rectangle that cover the peak displacements.

4. Discussion

4.1. Post-Observation Numbers and Atmospheric Correction

As the reconstruction requires multiple observations either side of the event time, it is important to know how many acquisitions are required to achieve a reliable estimation of coseismic offset within uncertainty. Given the large archive of Sentinel-1 data that is being amassed, the required pre-observations can be flexible (depending on the noise characteristic or the time series fitting model used) and may vary for different scenarios and study purposes. What we consider here is the number of post-earthquake observations required for a stable earthquake solution. Due to the long revisit time (≥6 days now), it would be of little value if we needed to wait many months or even years to collect enough images to obtain a high SNR reconstruction. A key factor here is the magnitude of atmospheric noise, as it is one of the main error sources of InSAR. To determine the relationship between the quality of reconstruction, the post-observations numbers, and the level of atmospheric noise, we calculate the change of standard errors (SEs) of the fitted coseismic displacements as we increase the use of post-observations during fitting for both tracks, with and without applying GACOS corrections first.

The quality of reconstruction improves both with the application of GACOS corrections (average 24.1% SEs reduction) and the increase of post-observation numbers used (Figure 5). The M_w 6.3 earthquake is a

special case as subsequent data are also used to fit the M_w 5.6 earthquake from the seventh post-observation onwards (the green dash line on Figure 5), causing its SEs to be fixed from that point forward. The low SEs at that point indicates the good quality of the reconstruction and also explains why these two earthquakes can be separated, although they are close in time and space. We determine the average number of post-observations for reaching a threshold, where the SE is 10% above its minimum value, is 14 acquisitions. This suggests our approach will achieve a stable output after around 3 months from the event time (assuming the revisit time is 6 days) in our study area. The number of acquisitions for other areas, with different noise characteristics, may vary somewhat.

4.2. Long-Term Linear Deformation Rate

For most of the pixels, the obtained long-term linear deformation rates are less than 10 mm/year (Figure S12). However, considering InSAR can only acquire relative displacements to the reference point, the long-term deformation rates we measured are noticeably above the level of interseismic deformation rate expected from the recent strain-rate map of our study area derived from GNSS data (Khorrami et al., 2019). One of the main reasons for this difference may come from using a constant linear rate in Equation 2. The linear deformation rate may be markedly changed after the mainshock according to time series, which potentially biases the estimation of the interseismic deformation rate and consequently the coseismic offset. In addition, the long-term rates may be associated with several other sources. First, non-tectonic deformation, such as that from hydrologically driven subsidence within basins is likely in this region. Second, topographically correlated atmosphere can map in as we do not include a seasonal term in the fitting. Third, a cumulated bias for linear rate estimation in time series may be expected from the use of short period interferograms (Ansari et al., 2021). Finally, discontinuities from phase unwrapping errors or any observation gap can have a significant impact on linear rate evaluation.

4.3. Implications of Our Approach

The primary use of our approach is to improve the InSAR detectability such that very small earthquakes ($M_w < 5.0$) may be observed when they reach to the surface (e.g., Lohman & Simons, 2005; Qian et al., 2019), and refine the deformation signal of earthquakes with low SNR. Due to the poor constraints of precise fault location by seismological observations in regions of low instrumentation (Husen & Hardebeck, 2010), this will be useful for improving the identification of active faults within continental areas lacking dense seismic coverage.

Our approach can also be used to enhance the complex signals of large earthquakes ($M_w \geq 6.5$), reducing extra noise as we have done with smaller earthquakes. In addition, it can disentangle coseismic signals from the postseismic signal that occurred before the first post-acquisition due to the latency of SAR acquisition (Floyd et al., 2016; Twardzik et al., 2019; Zinke et al., 2014), useful for the analysis of both coseismic and postseismic deformations and avoiding any possible systematic bias in subsequent earthquake modeling (Weston et al., 2012).

Further applications of our approach include splitting up complex sequences of earthquakes (especially aftershock sequences as we have done here), and possibly studying small-amplitude signals from large, deep earthquakes within subduction zones (Barnhart et al., 2014).

5. Conclusions

We demonstrate the use of InSAR time series analysis for detecting and modeling aftershocks in the presence of the postseismic signal following a major earthquake that otherwise might go undetected within single interferograms. We develop an approach using reconstructed coseismic deformation fields to enhance the surface displacement signals and subsequently to better constrain the earthquake modeling, in particular location and depth. We show that our time series approach improves on noise reduction using additional acquisitions following an earthquake, and achieves a stable result with 14 post-observations in this study area. We conclude that a time series approach is effective for enhancing the InSAR resolving power for earthquake studies, and outline its possible applications for the future.

Data Availability Statement

The Sentinel-1 SAR data are copyrighted by the European Space Agency and additionally distributed by the Alaska Satellite Facility Distributed Active Archive Center (https://earthdata.nasa.gov/eosdis/daacs/asf). The processed InSAR interferograms used in this work are available at COMET-LiCS Sentinel-1 InSAR portal (https://comet.nerc.ac.uk/COMET-LiCS-portal/).

Acknowledgments
This work is supported by the UK Natural Environment Research Council (NERC) through the Centre for the Observation and Modeling of Earthquakes, Volcanoes and Tectonics (COMET, http://comet.nerc.ac.uk), and the Continents from Space (LiCS) large Grant (NE/K010867/1). We use seismological observations from the United States Geological Survey (https://www.usgs.gov), the Global Centroid-Moment-Tensor (https://www.gcmt.org.uk), and the International Seismological Centre (International Seismological Centre, 2021; http://www.isc.ac.uk). Figures are made using the Generic Mapping Tools (GMT) (Wessel et al., 2013). John Elliott acknowledges support from the Royal Society through a University Research Fellowship (UF150282). Tim Craig thanks the Royal Society for support through URF\R1\180088.

References

Agram, P. S., & Simons, M. (2015). A noise model for InSAR time series. *Journal of Geophysical Research: Solid Earth*, *120*, 2752–2771. https://doi.org/10.1002/2014JB011271

Ambraseys, N. N. (2001). Reassessment of earthquakes, 1900–1999, in the Eastern Mediterranean and the Middle East. *Geophysical Journal International*, *145*(2), 471–485. https://doi.org/10.1046/j.0956-540x.2001.01396.x

Ansari, H., De Zan, F., & Parizzi, A. (2021). Study of systematic bias in measuring surface deformation with SAR interferometry. *IEEE Transactions on Geoscience and Remote Sensing*, *59*(2), 1285–1301. https://doi.org/10.1109/TGRS.2020.3003421

Bagnardi, M., & Hooper, A. (2018). Inversion of surface deformation data for rapid estimates of source parameters and uncertainties: A Bayesian approach. *Geochemistry, Geophysics, Geosystems*, *19*(7), 2194–2211. https://doi.org/10.1029/2018GC007585

Barnhart, W. D., Brengman, C. M. J., Li, S., & Peterson, K. E. (2018). Ramp-flat basement structures of the Zagros Mountains inferred from co-seismic slip and afterslip of the 2017 M_w 7.3 Darbandikhan, Iran/Iraq earthquake. *Earth and Planetary Science Letters*, *496*, 96–107. https://doi.org/10.1016/j.epsl.2018.05.036

Barnhart, W. D., Hayes, G. P., Samsonov, S. V., Fielding, E. J., & Seidman, L. E. (2014). Breaking the oceanic lithosphere of a subducting slab: The 2013 Khash, Iran earthquake. *Geophysical Research Letters*, *41*(1), 32–36. https://doi.org/10.1002/2013GL058096

Bekaert, D. P. S., Walters, R. J., Wright, T. J., Hooper, A. J., & Parker, D. J. (2015). Statistical comparison of InSAR tropospheric correction techniques. *Remote Sensing of Environment*, *170*, 40–47. https://doi.org/10.1016/j.rse.2015.08.035

Biggs, J., Bergman, E., Emmerson, B., Funning, G. J., Jackson, J., Parsons, B., & Wright, T. J. (2006). Fault identification for buried strike-slip earthquakes using InSAR: The 1994 and 2004 Al Hoceima, Morocco earthquakes. *Geophysical Journal International*, *166*(3), 1347–1362. https://doi.org/10.1111/j.1365-246X.2006.03071.x

Copley, A., Karasozen, E., Oveisi, B., Elliott, J. R., Samsonov, S., & Nissen, E. (2015). Seismogenic faulting of the sedimentary sequence and laterally variable material properties in the Zagros Mountains (Iran) revealed by the August 2014 murmuri (E. Dehloran) earthquake sequence. *Geophysical Journal International*, *203*(2), 1436–1459. https://doi.org/10.1093/gji/ggv365

Copley, A., & Reynolds, K. (2014). Imaging topographic growth by long-lived postseismic afterslip at Sefidabeh, east Iran. *Tectonics*, *33*, 330–345. https://doi.org/10.1002/2013TC003462

Crosetto, M., Monserrat, O., Cuevas-González, M., Devanthéry, N., & Crippa, B. (2016). Persistent scatterer interferometry: A review. *ISPRS Journal of Photogrammetry and Remote Sensing*, *115*, 78–89. https://doi.org/10.1016/j.isprsjprs.2015.10.011

Dalaison, M., & Jolivet, R. (2020). A Kalman filter time series analysis method for InSAR. *Journal of Geophysical Research: Solid Earth*, *125*, e2019JB019150. https://doi.org/10.1029/2019JB019150

Doin, M. P., Lasserre, C., Peltzer, G., Cavalié, O., & Doubre, C. (2009). Corrections of stratified tropospheric delays in SAR interferometry: Validation with global atmospheric models. *Journal of Applied Geophysics*, *69*(1), 35–50. https://doi.org/10.1016/j.jappgeo.2009.03.010

Elliott, J. R., Walters, R. J., England, P. C., Jackson, J. A., Li, Z., & Parsons, B. (2010). Extension on the Tibetan plateau: Recent normal faulting measured by InSAR and body wave seismology. *Geophysical Journal International*, *183*(2), 503–535. https://doi.org/10.1111/j.1365-246X.2010.04754.x

Elliott, J. R., Walters, R. J., & Wright, T. J. (2016). The role of space-based observation in understanding and responding to active tectonics and earthquakes. *Nature Communications*, *7*(1). https://doi.org/10.1038/ncomms13844

England, P., & Jackson, J. (2011). Uncharted seismic risk. *Nature Geoscience*, *4*(6), 348–349. https://doi.org/10.1038/ngeo1168

Fathian, A., Atzori, S., Nazari, H., Reicherter, K., Salvi, S., Svigkas, N., et al. (2021). Complex co- and postseismic faulting of the 2017–2018 seismic sequence in western Iran revealed by InSAR and seismic data. *Remote Sensing of Environment*, *253*, 112224. https://doi.org/10.1016/j.rse.2020.112224

Feng, W., Samsonov, S., Almeida, R., Yassaghi, A., Li, J., Qiu, Q., et al. (2018). Geodetic constraints of the 2017 M_w7.3 Sarpol Zahab, Iran earthquake, and its implications on the structure and mechanics of the northwest Zagros thrust-fold belt. *Geophysical Research Letters*, *45*(14), 6853–6861. https://doi.org/10.1029/2018GL078577

Ferretti, A., Fumagalli, A., Novali, F., Prati, C., Rocca, F., & Rucci, A. (2011). A new algorithm for processing interferometric data-stacks: SqueeSAR. *IEEE Transactions on Geoscience and Remote Sensing*, *49*(9), 3460–3470. https://doi.org/10.1109/TGRS.2011.2124465

Fialko, Y. (2006). Interseismic strain accumulation and the earthquake potential on the southern San Andreas fault system. *Nature*, *441*(7096), 968–971. https://doi.org/10.1038/nature04797

Fielding, E. J., Sangha, S. S., Bekaert, D. P. S., Samsonov, S. V., & Chang, J. C. (2017). Surface deformation of North-Central Oklahoma related to the 2016 M_w 5.8 Pawnee earthquake from SAR interferometry time series. *Seismological Research Letters*, *88*(4), 971–982. https://doi.org/10.1785/0220170010

Floyd, M. A., Walters, R. J., Elliott, J. R., Funning, G. J., Svarc, J. L., Murray, J. R., et al. (2016). Spatial variations in fault friction related to lithology from rupture and afterslip of the 2014 South Napa, California, earthquake. *Geophysical Research Letters*, *43*(13), 6808–6816. https://doi.org/10.1002/2016GL069428

Funning, G. J., & Garcia, A. (2019). A systematic study of earthquake detectability using Sentinel-1 Interferometric Wide-swath data. *Geophysical Journal International*, *216*(1), 332–349. https://doi.org/10.1093/gji/ggy426

Goldstein, R. M., & Werner, C. L. (1998). Radar interferogram filtering for geophysical applications. *Geophysical Research Letters*, *25*(21), 4035–4038. https://doi.org/10.1029/1998GL900033

Grandin, R., Vallée, M., & Lacassin, R. (2017). Rupture process of the M_w 5.8 Pawnee, Oklahoma, earthquake from Sentinel-1 InSAR and seismological data. *Seismological Research Letters*, *88*(4), 994–1004. https://doi.org/10.1785/0220160226

Heflin, M., Donnellan, A., Parker, J., Lyzenga, G., Moore, A., Grant Ludwig, L., et al. (2020). Automated estimation and tools to extract positions, velocities, breaks, and seasonal terms from daily GNSS measurements: Illuminating nonlinear Salton Trough deformation. *Earth and Space Science*, *7*(7). https://doi.org/10.1029/2019EA000644

Hilley, G. E., Bürgmann, R., Ferretti, A., Novali, F., & Rocca, F. (2004). Dynamics of slow-moving landslides from permanent scatterer analysis. *Science*, *304*(5679), 1952–1955. https://doi.org/10.1126/science.1098821

Hooper, A., Bekaert, D., Spaans, K., & Arikan, M. (2012). Recent advances in SAR interferometry time series analysis for measuring crustal deformation. *Tectonophysics*, *514–517*, 1–13. https://doi.org/10.1016/j.tecto.2011.10.013

Hooper, A., Segall, P., & Zebker, H. (2007). Persistent scatterer interferometric synthetic aperture radar for crustal deformation analysis, with application to Volcán Alcedo, Galápagos. *Journal of Geophysical Research: Solid Earth*, *112*(7), 1–21. https://doi.org/10.1029/2006JB004763

Husen, S., & Hardebeck, J. L. (2010). Earthquake location accuracy, Community Online Resource for Statistical Seismicity Analysis. https://doi.org/10.5078/corssa-55815573

Ide, S. (2019). Frequent observations of identical onsets of large and small earthquakes. *Nature*, *573*(7772), 112–116. https://doi.org/10.1038/s41586-019-1508-5

Ingleby, T., & Wright, T. J. (2017). Omori-like decay of postseismic velocities following continental earthquakes. *Geophysical Research Letters*, *44*(7), 3119–3130. https://doi.org/10.1002/2017GL072865

International Seismological Centre. (2021). On-line bulletin. https://doi.org/10.31905/D808B830

Jolivet, R., Lasserre, C., Doin, M.-P., Guillaso, S., Peltzer, G., Dailu, R., et al. (2012). Shallow creep on the Haiyuan Fault (Gansu, China) revealed by SAR interferometry. *Journal of Geophysical Research: Solid Earth*, *117*, B06401. https://doi.org/10.1029/2011JB008732

Khorrami, F., Vernant, P., Masson, F., Nilfouroushan, F., Mousavi, Z., Nankali, H., et al. (2019). An up-to-date crustal deformation map of Iran using integrated campaign-mode and permanent GPS velocities. *Geophysical Journal International*, *217*(2), 832–843. https://doi.org/10.1093/gji/ggz045

Lazecky, M., Spaans, K., Gonzalez, P. J., Maghsoudi, Y., Morishita, Y., Albino, F., et al. (2020). LiCSAR: An automatic InSAR tool for measuring and monitoring tectonic and volcanic activity. *Remote Sensing*, *12*, 2430. https://doi.org/10.3390/rs12152430

Li, Z., Muller, J.-P., Cross, P., & Fielding, E. J. (2005). Interferometric synthetic aperture radar (InSAR) atmospheric correction: GPS, Moderate Resolution Imaging Spectroradiometer (MODIS), and InSAR integration. *Geophysical Research Letters*, *110*, B03410. https://doi.org/10.1029/2004JB003446

Liu, X., & Xu, W. (2019). Logarithmic model joint inversion method for coseismic and postseismic slip: Application to the 2017 M_w 7.3 Sarpol Zahāb earthquake, Iran. *Journal of Geophysical Research: Solid Earth*, *124*(11), 12034–12052. https://doi.org/10.1029/2019JB017953

Lohman, R. B., & Simons, M. (2005). Locations of selected small earthquakes in the Zagros Mountains. *Geochemistry, Geophysics, Geosystems*, *6*(3). https://doi.org/10.1029/2004GC000849

Luo, H., Wang, T., Wei, S., Liao, M., & Gong, J. (2021). Deriving centimeter-level coseismic deformation and fault geometries of small-to-moderate earthquakes from time-series Sentinel-1 SAR images. *Frontiers of Earth Science*, *9*. https://doi.org/10.3389/feart.2021.636398

Massonnet, D., Rossi, M., Carmona, C., Adragna, F., Peltzer, G., Feigl, K., & Rabaute, T. (1993). The displacement field of the Landers earthquake mapped by radar interferometry. *Nature*, *364*, 138–142. https://doi.org/10.1038/364138a0

Morishita, Y. (2019). A systematic study of synthetic aperture radar interferograms produced from ALOS-2 data for large global earthquakes from 2014 to 2016. *IEEE Journal of Selected Topics in Applied Earth Observations and Remote Sensing*, *12*(7), 2397–2408. https://doi.org/10.1109/jstars.2019.2921664

Nissen, E., Ghods, A., Karasözen, A., Elliott, J. R., Barnhart, W. D., Bergman, E. A., et al. (2019). The 12 November 2017 M_w 7.3 Ezgeleh-Sarpolzahab (Iran) earthquake and active tectonics of the Lurestan Arc. *Journal of Geophysical Research: Solid Earth*, *124*, 2124–2152. https://doi.org/10.1029/2018JB016221

Okada, Y. (1985). Surface deformation due to shear and tensile faults in a half-space. *Bulletin of the Seismological Society of America*, *75*(4), 1135–1154.

Osmanoğlu, B., Sunar, F., Wdowinski, S., & Cabral-Cano, E. (2016). Time series analysis of InSAR data: Methods and trends. *ISPRS Journal of Photogrammetry and Remote Sensing*, *115*, 90–102. https://doi.org/10.1016/j.isprsjprs.2015.10.003

Pedersen, R., Jónsson, S., Árnadóttir, T., Sigmundsson, F., & Feigl, K. L. (2003). Fault slip distribution of two June 2000 M_w 6.5 earthquakes in South Iceland estimated from joint inversion of InSAR and GPS measurements. *Earth and Planetary Science Letters*, *213*(3–4), 487–502. https://doi.org/10.1016/S0012-821X(03)00302-9

Peltzer, G., & Rosen, P. (1995). Surface displacement of the 17 May 1993 Eureka Valley, California, earthquake observed by SAR interferometry. *Science*, *268*(5215), 1333–1336. https://doi.org/10.1126/science.268.5215.1333

Pepe, A., Yang, Y., Manzo, M., & Lanari, R. (2015). Improved EMCF-SBAS processing chain based on advanced techniques for the noise-filtering and selection of small baseline multi-look DInSAR interferograms. *IEEE Transactions on Geoscience and Remote Sensing*, *53*(8), 4394–4417. https://doi.org/10.1109/TGRS.2015.2396875

Qian, Y., Chen, X., Luo, H., Wei, S., Wang, T., Zhang, Z., & Luo, X. (2019). An extremely shallow M_w 4.1 thrust earthquake in the eastern Sichuan Basin (China) likely triggered by unloading during infrastructure construction. *Geophysical Research Letters*, *46*(23), 13775–13784. https://doi.org/10.1029/2019gl085199

Ryder, I., Parsons, B., Wright, T. J., & Funning, G. J. (2007). Post-seismic motion following the 1997 Manyi (Tibet) earthquake: InSAR observations and modelling. *Geophysical Journal International*, *169*(3), 1009–1027. https://doi.org/10.1111/j.1365-246X.2006.03312.x

Salvi, S., Stramondo, S., Funning, G. J., Ferretti, A., Sarti, F., & Mouratidis, A. (2012). The Sentinel-1 mission for the improvement of the scientific understanding and the operational monitoring of the seismic cycle. *Remote Sensing of Environment*, *120*, 164–174. https://doi.org/10.1016/j.rse.2011.09.029

Samiei-Esfahany, S., Martins, J. E., Van Leijen, F., & Hanssen, R. F. (2016). Phase estimation for distributed scatterers in InSAR stacks using integer least squares estimation. *IEEE Transactions on Geoscience and Remote Sensing*, *54*(10), 5671–5687. https://doi.org/10.1109/TGRS.2016.2566604

Scholz, C. (2002). *The mechanics of earthquakes and faulting* (2nd ed.). Cambridge University Press. https://doi.org/10.1017/CBO9780511818516

Styron, R., & Pagani, M. (2020). The GEM Global Active Faults Database. *Earthquake Spectra*, *36*(1_suppl), 160–180. https://doi.org/10.1177/8755293020944182

Tobita, M. (2016). Combined logarithmic and exponential function model for fitting postseismic GNSS time series after 2011 Tohoku-Oki earthquake. *Earth Planets and Space*, *68*(1), 41. https://doi.org/10.1186/s40623-016-0422-4

Twardzik, C., Vergnolle, M., Sladen, A., & Avallone, A. (2019). Unravelling the contribution of early postseismic deformation using sub-daily GNSS positioning. *Scientific Reports*, *9*(1). https://doi.org/10.1038/s41598-019-39038-z

Webster, R., & Oliver, M. A. (2007). *Geostatistics for environmental scientists* (2nd ed.). John Wiley & Sons. https://doi.org/10.1002/9780470517277

Wessel, P., Smith, W. H. F., Scharroo, R., Luis, J., & Wobbe, F. (2013). Generic mapping tools: Improved version released. *Eos*, *94*(45), 409–410. https://doi.org/10.1002/2013EO450001

Weston, J., Ferreira, A. M. G., & Funning, G. J. (2012). Systematic comparisons of earthquake source models determined using InSAR and seismic data. *Tectonophysics*, *532-535*, 61–81. https://doi.org/10.1016/j.tecto.2012.02.001

Yu, C., Li, Z., Penna, N. T., & Crippa, P. (2018). Generic atmospheric correction model for interferometric synthetic aperture radar observations. *Journal of Geophysical Research: Solid Earth*, *123*(10), 9202–9222. https://doi.org/10.1029/2017JB015305

Zebker, H. A., Rosen, P. A., & Hensley, S. (1997). Atmospheric effects in interferometric synthetic aperture radar surface deformation and topographic maps. *Journal of Geophysical Research: Solid Earth*, *102*(B4), 7547–7563. https://doi.org/10.1029/96JB03804

Zinke, R., Hollingsworth, J., & Dolan, J. F. (2014). Surface slip and off-fault deformation patterns in the 2013 M_w 7.7 Balochistan, Pakistan earthquake: Implications for controls on the distribution of near-surface coseismic slip. *Geochemistry, Geophysics, Geosystems*, *15*(12), 5034–5050. https://doi.org/10.1002/2014GC005538